nature portfolio

https://doi.org/10.1038/s41587-021-00948-x

Supplementary information

Fully implantable and bioresorbable cardiac pacemakers without leads or batteries

In the format provided by the authors and unedited

Supplementary Information

Fully implantable and bioresorbable cardiac pacemakers without leads or batteries

Yeon Sik Choi, Rose T. Yin, Anna Pfenniger, Jahyun Koo, Raudel Avila, K. Benjamin Lee, Sheena W. Chen, Geumbee Lee, Gang Li, Yun Qiao, Alejandro Murillo-Berlioz, Alexi Kiss, Shuling Han, Seung Min Lee, Chenhang Li, Zhaoqian Xie, Yu-Yu Chen, Amy Burrell, Beth Geist, Hyoyoung Jeong, Joohee Kim, Hong-Joon Yoon, Anthony Banks, Seung-Kyun Kang, Zheng Jenny Zhang, Chad R. Haney, Alan Varteres Sahakian, David Johnson, Tatiana Efimova, Yonggang Huang, Gregory D. Trachiotis, Bradley P. Knight, Rishi K. Arora, Igor R. Efimov, John A. Rogers

Contents

Supplementary Note 1. Low frequency *PIN* diode for capacitor-free design

Here, a bioresorbable low-frequency *PIN* diode with high parasitic capacitance yields a capacitor-free bioresorbable electrical stimulator with enhanced output performance. With the *PIN* structured diode in reverse bias, charge accumulates at the *PI* and *IN* junctions, thereby creating a diode capacitance (C_t) where the *I* region acts as a parasitic capacitor with capacitance proportional to the area (A) and inversely proportional to the distance (d)[1]. When forward biased, the *PIN* diode acts as a variable resistor. Switching between reverse and forward bias at timescales much larger than the carriers' lifetime leads to the typical behavior of a diode. However, the diodes have a reverse-recovery time, corresponding to a time for changing its response to a forward-biased from a reverse-biased state. Such switching results in some current flow in the reverse direction, and the reverse-recovery time is proportional to the size of C_t. Based on this mechanism, the bioresorbable *PIN* diode can be designed with a reverse-recovery time of the order of microseconds. At high-frequency (> 1 MHz), the diode cannot fully recover during switching, thereby yielding DC-like output (with ripples) without the need for a smoothing capacitor. To illustrate the electrical characteristics of capacitor-free device with low-frequency *PIN* diode, we implemented the circuit shown in Fig. S1a. At low input frequency (100 Hz), the voltage at the load resistor shows a typical AC-like half-cycle signal (Fig. S1b) representative of a half-wave rectifier. However, at high input frequency (14.8 MHz), the output voltage at the load shows a low amplitude AC-signal on a DC offset (Fig. S1c). The transition from an AC-like half-cycle to DC-like ripples occurs at around 1 MHz input frequency. The device with a bioresorbable capacitor (47 pF) shows an open circuit voltage (V_{oc}) of ~ 6 V at a resonance frequency of 6.1 MHz (Fig. S1d), while capacitor-free device shows V_{oc} of ~ 10 V at a resonance frequency of 13.5 MHz (Fig. S1e). This result indicates that the capacitor-free device supports improved performance since the output voltage (V_0) is as follows:

$$V_o = 2\pi\, f\, N\, S\, Q\, B_o\, \cos\alpha$$

where f is the frequency of the input signal, N is the number of turns of coil in the loop, S is the area of the loop, Q is the quality factor of circuit, B_O is the strength of the input signal, and α is the angle of arrival of the signal[2]. In addition, eliminating the capacitor component, simplifying the

fabrication process, and reducing the number of interconnections further improves the yields and mechanical reliability of the device.

Supplementary Note 2. Electrode spacing optimization using a cable model

The one-dimensional cable theory is a useful mathematical model where a "cable" with specific electrical properties approximates the dynamics of a "strip" of myocardium. Using the cable theory model, we can garner some qualitative insights into the optimal electrode design for electrode-induced myocardial excitation[3]. According to cable theory, we can model the extracellular space around the myocyte as a cylinder of radius of d_{e-m}, or the distance between the electrode and the excitable myocardium (Fig. S3). Only a small portion of the electric current applied at the electrodes passes through to the cell membrane and into the cell, and the magnitude of the transmembrane current flow depends on the relative resistance of the intracellular and extracellular fluids. Here, the extracellular resistance (R_{ext}) can be defined as follows[3]:

$$R_{ext} = \frac{1}{\pi\, d_{e-m}^2\, G_{out}}$$

where G_{out} is the extracellular fluid conductivity. The interelectrode extracellular fluid potential difference ($\Delta\Psi_{out}$) is also the minimum voltage that must be applied across the electrodes to achieve myocardial capture which can be expressed by[3]

$$\Delta\Psi_{out} = I_0\, R_{ext}\, L = \frac{I_0\, L}{\pi\, {d_{e-m}}^2\, G_{out}}$$

$$\Rightarrow L = \frac{\Delta\Psi_{out}\, \pi\, d_{e-m}^2\, G_{out}}{I_0}$$

where I_0 is the threshold current and L is the interelectrode distance. For the same minimum input voltage for pacing ($\Delta\Psi_{out}$) where G_{out} and I_0 are relatively constant across scenarios, this equation suggests that the interelectrode distance (L) primarily depends the distance between the electrode and excitable myocardium (d_{e-m}). Since animals with larger hearts have a greater d_{e-m} as evidenced by a greater tissue impedance, a greater L is required for large animals compared to small animals[4–6]. Based on this approximation, we tune the electrode spacing between 1 mm to 5 mm depending on the size of the hearts.

Supplementary Note 3. Device design optimization for long-range wireless operation

The coil-to-coil distance is a critical factor that affects the power transfer efficiency in a wireless induction scheme[7]. For example, for a fixed input voltage (i.e. transmitting voltage) of 10 V_{pp} at the Tx coil, the output voltage at the Rx coil decreases from 16 V to 0.2 V with respect to distances from 1 mm to 8 mm (Extended Data Fig. 4g). Fig. S7a and S7b show simulated scattering parameters (S11) and Q factors of the wireless power harvesting units with four different sizes of Rx coils: 25 (blue), 18 (red), 12 (black), and 8 mm (green). Fig. S7c shows that the largest coil (25 mm) generates much higher output voltage (~14.8 V) than the smallest (8 mm) coils (~2.12 V) at the same input voltage of 10 V_{pp} and load resistance of 5 kΩ, as expected with scaling with the area defined by the coil. The results in Fig. S7d show that increasing the size of the Rx coil proportionally increases energy transfer efficiency. The design of the Tx coil is also important for enhancing wireless power transfer. Fig. S8 shows the results of *in vitro* tests of the energy transfer capabilities of the bioresorbable pacemaker system with various Tx coils (Fig. S8a): (i) Tx coil I (solenoid type; 3 turns; 12 mm diameter); (ii) Tx coil II (solenoid type; 4 turns; 100 mm diameter); Tx coil III (square; 1 turn; 260 × 280 mm^2). Slices of pig tissue with thicknesses between 20 and 120 mm, including skin, fat, bone, and muscle, served as a mock compound inserted between the Tx coil and the device (Fig. S8b-d). As shown in Fig. S8e, Tx coil I can deliver a power of 13.5 mW (input power = 12 W; resonance frequency = 13.56 MHz; load resistance = 5 kΩ) at a distance of up to 6 cm. In contrast, Tx coil III can deliver a much higher power (32.8 mW) at much large distances (up to 20 cm) in otherwise similar testing conditions (Fig. S8g). These results indicate that this system can support long-range operation in cardiac pacing. *In vivo* acute pacing tests in a canine model shows results that are consistent with *in vitro* tests (Fig. S9). As shown in Fig. S9a and 9b, we monitor the changes in the ECG as a function of coil-to-coil distance to define the maximum pacing distance (i.e. the largest distance between the skin and the Tx coil that enables consistent ventricular capture) at various input powers between 2 and 12 W. Fig. S9c shows that the maximum distance is around 17 cm at input power of 12 W. Considering that the distance between the implanted Rx coil and the surface of the skin around 3 cm, the maximum distance between Rx and Tx coils can be 20 cm. Taken together, these results show that the Rx to Tx coil distance and design of the Tx coil impact the parameters for optimal power transfer. In consideration of the translation of these results for patients, these parameters can be selected to tailor to clinical case needs for optimal power transfer at the minimum transmitting voltages.

Supplementary Note 4. Clinical case scenario

Although many parameters contribute to stable pacing, including input frequency, input power, pulse width, burst period, and coil-to-coil distance, optimization of the wireless energy transfer system simplifies the operation. The designs of the Rx and Tx coils are optimized for operation at a fixed input frequency of 13.56 MHz. Studies using the canine model provide guidelines for the maximum pacing distance for a given input power. The pulse width and burst period can be predefined or manipulated during pacing using insights from the patient's ECG signals and therapeutic treatment strategy. Since the cardiac pacing follows an all-or-nothing threshold behavior, users can change one parameter, such as input power or coil-to-coil distance, until changes in ECG signal indicate a transition from intrinsic to pacing rhythm.

Supplementary Note 5. Encapsulation materials for long-term operation

The encapsulation materials and their thickness define the functional lifetime of the devices. Although bioresorbable wax (Candelilla wax) can be considered[8], its poor mechanical properties and the relatively high melting temperature (~ 70°C) needed for dip-coating-based encapsulation process limit its feasibility for use with bioresorbable electrical stimulators. A hydrophobic polyanhydride (polybuthanedithiol 1,3,5-triallyl-1,3,5-triazine-2,4,6(1H,3H,5H)-trione pentenoic anhydride, PBTPA)[9] can serve as an attractive alternative for an advanced encapsulation structure to allow for long functional lifetimes. The encapsulation process involves placing the device on a partially cured layer of PBTPA and subsequently UV-curing after applying a liquid mixture of precursors on the top. The result is a conformal encapsulation structure with a thickness of approximately 300 μm. This UV-based photocuring process does not damage the bioresorbable devices because it occurs at room temperature, well below the glass transition temperature of the PLGA. Fig. S13 shows the mechanical reliability of bioresorbable cardiac pacemaker with wax or PBTPA encapsulations before and after mechanical bending. Many cracks occur on the wax-encapsulated extension electrode after bending (bend radius = 10 mm) due to the mechanical rigidity of the Candelilla wax, and wax encapsulation is delaminated by bending (bend radius = 5 mm). In contrast, PBTPA encapsulations maintain their structure before and after mechanical deformation. Fig. S14 shows results of benchtop tests of the water-barrier properties of this encapsulating structure, as demonstrated by the functional lifetime of the wireless, bioresorbable cardiac pacemaker. Soak testing in bovine serum at 37 °C for 25 days reveals stable operation throughout due to the water barrier properties of the hydrophobic chains of the PBTPA. The barrier characteristics can be further enhanced by increasing the thickness of the PBTPA[9].

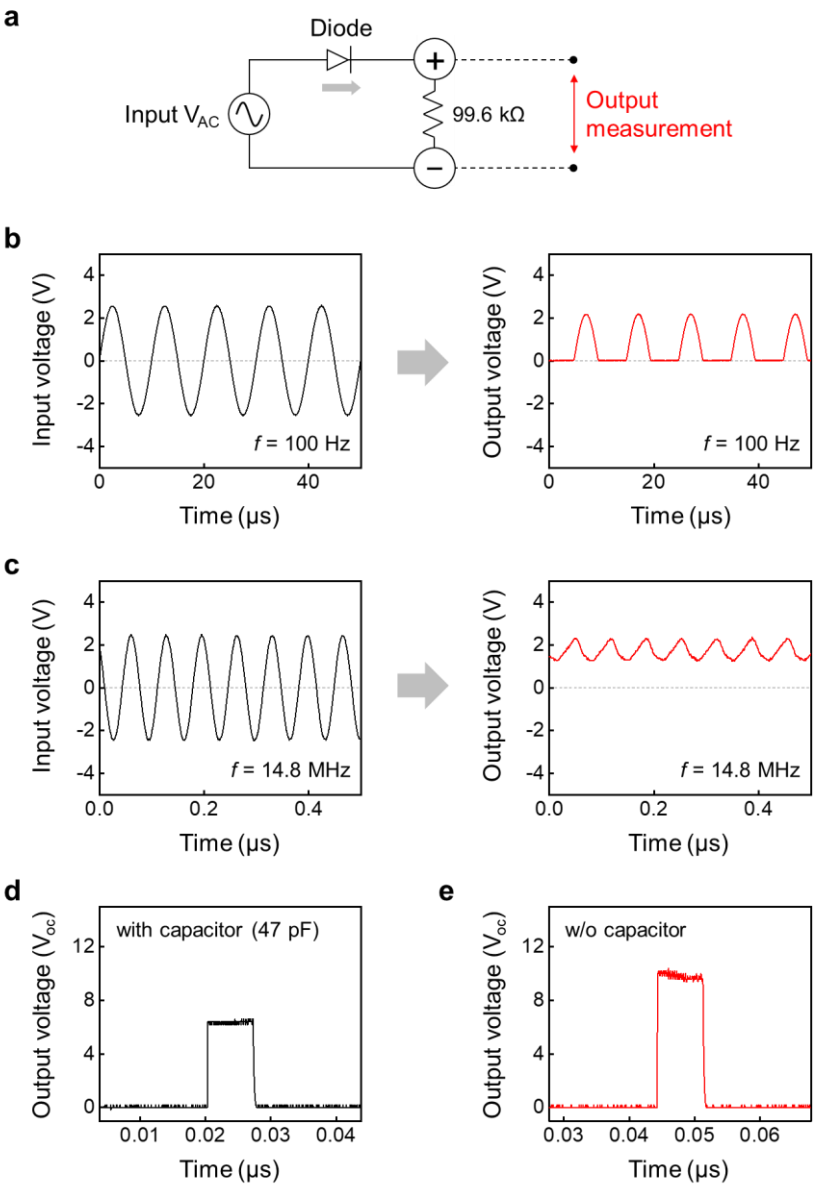

Supplementary Fig. 1 | Input frequency dependent behavior of a bioresorbable diode.

a, Schematic illustration of the circuit diagram for the characterization of the bioresorbable diode. Load resistance, 99.6 kΩ. **b,** Low frequency signal rectification performance of the bioresorbable diode: (left) input AC signal with frequency of 100 Hz; (right) rectified AC-like half-cycle signal. **c**, High frequency signal rectification performance of the bioresorbable diode: (left) input AC signal with frequency of 14.8 MHz; (right) rectified DC-like signal. **d**, Pulse output signal (open circuit voltage, V_{oc}) from the bioresorbable cardiac pacemaker with bioresorbable a capacitor (47 pF) (input voltage = 2 V_{pp}; input frequency = 6.1 MHz; frequency = 400 BPM; pulse width = 7 ms). **e**, Pulse output signal (V_{oc}) from the bioresorbable cardiac pacemaker without capacitor (input voltage = 2 V_{pp}; input frequency = 13.5 MHz frequency = 400 BPM; pulse width = 7 ms).

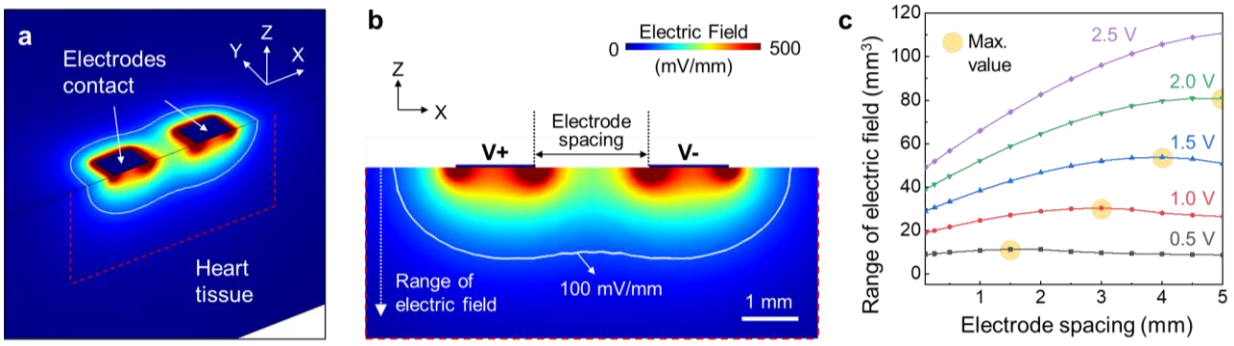

Supplementary Fig. 2 | Finite element analysis (FEA) simulations of the electric field distributions near the electrode-myocardium interface upon electrical stimulation

a, b, Computational results for distributions of the electric field within the cardiac tissue and relationships to design parameters associated with the contact electrodes in three-dimensional (3D) and two-dimensional (2D; x, z-axis) space, respectively. **c,** Simulated range of electric field as a function of electrode spacing with different input voltages at an electric field strength of 100 mV/mm (black, 0.5 V; red, 1.0 V; blue, 1.5 V; green, 2.0 V; violet, 2.5 V). The yellow circles indicate the maximum range of electric field and the corresponding electrode spacing at the specific input voltage. These results show that this bipolar electrode design generates a strong electric field and that transmitting voltages and interelectrode distance influence the range, and therefore strength, of the produced electric field.

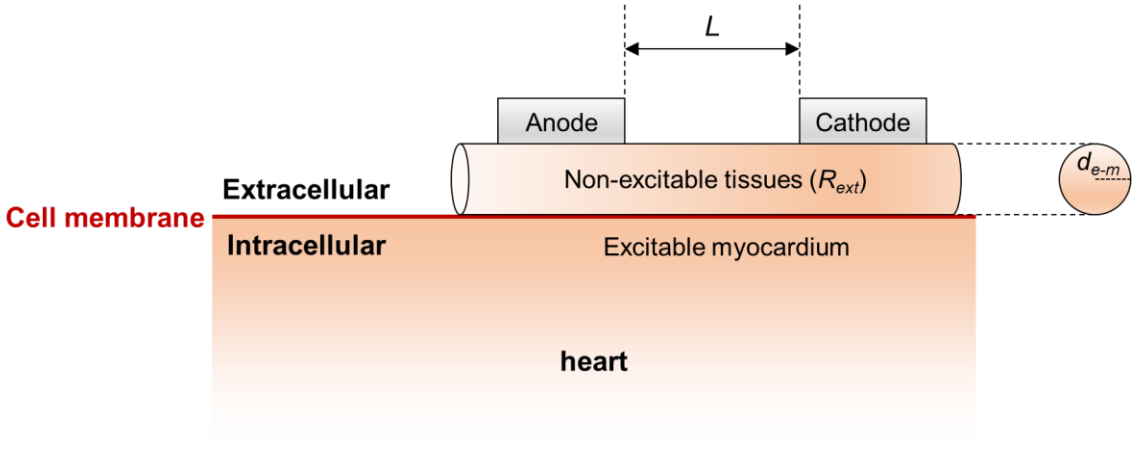

Supplementary Fig. 3 | Cable model of the process for stimulating excitable cells.

The cable model approximates a strip of cardiac tissue as a cable composed of resistors and capacitors to match specific electrical properties of the myocardium. The extracellular space that surrounds the excitable myocytes can be modeled as a cylinder with diameter $d_{e\text{-}m}$ and a resistance of R_{ext}. The potential difference of the interelectrode extracellular fluid is the minimum voltage that must be applied in order to capture the heart. Employment of this model determines the optimal distance (L) between contact electrodes for capture of the heart rhythm with minimum voltage input.

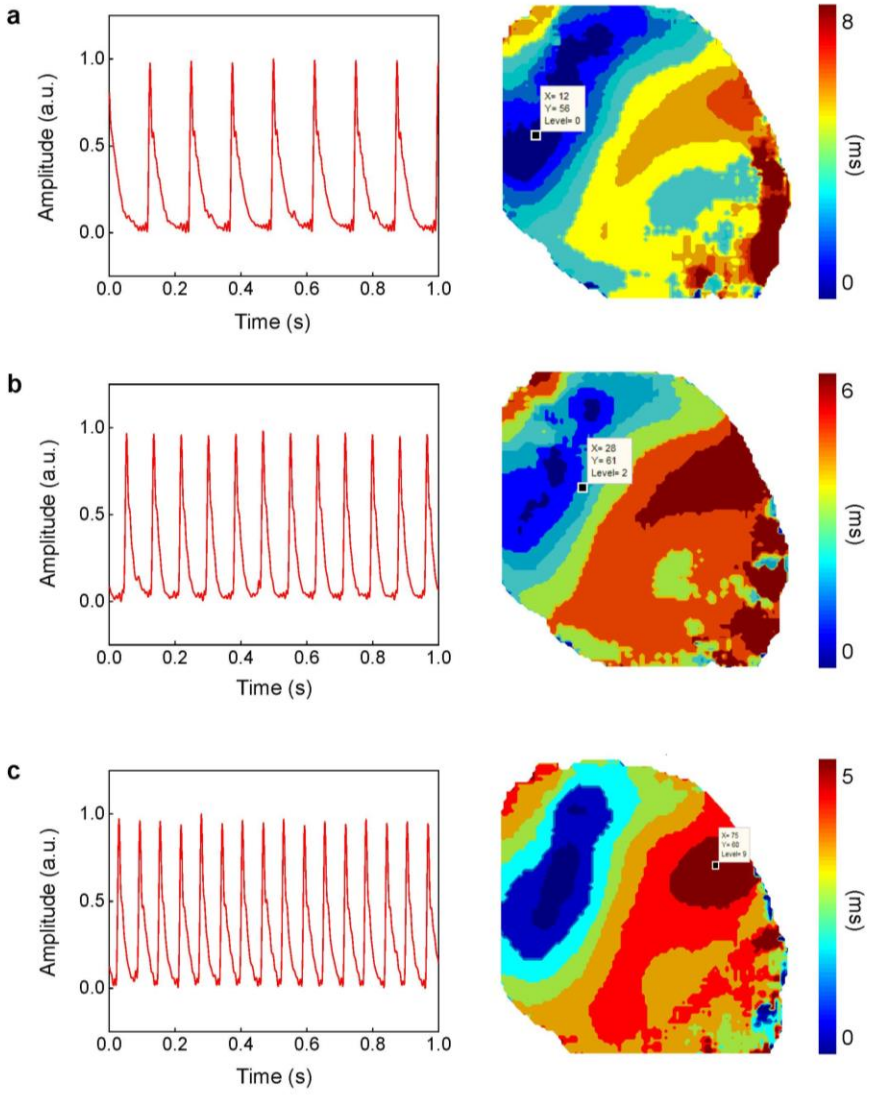

Supplementary Fig. 4 | *Ex vivo* demonstration of bioresorbable, leadless cardiac pacemaker on mouse at different pacing frequencies.

a, b, c, Representative optical action potential (left) and activation map (right) of a mouse heart during pacing with different pacing frequencies of 8, 12, and 16 Hz. Increasing the stimulation frequency maintains a 1 to 1 capture rate of stimulus to evoked action potential response with an appropriate increase in overall ventricular rate.

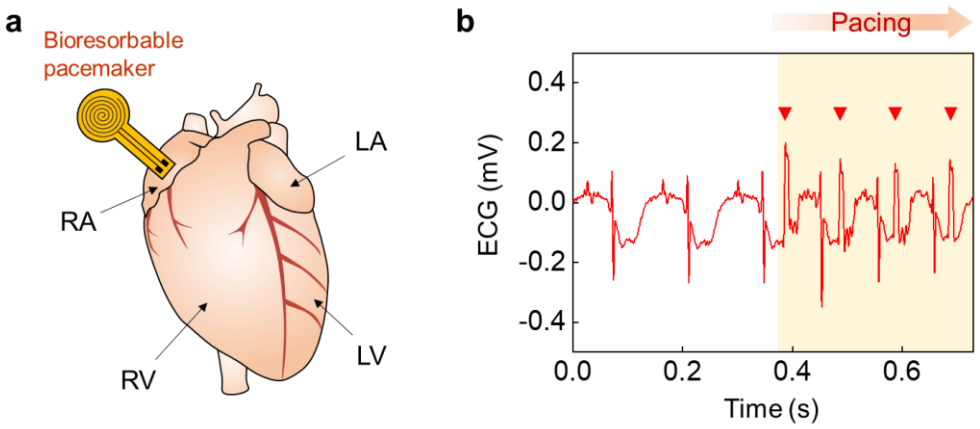

Supplementary Fig. 5 | *In vivo* demonstrations of atrial pacing by the bioresorbable cardiac pacemakers in a rat model.

a, Schematic illustration of the rat's heart and position of the bioresorbable pacemaker. **b,** ECG signals before (white background) and during electrical stimulation on right atrium (RA) (yellow background; red arrows indicate delivered electrical stimuli). n = 3 biologically independent animals.

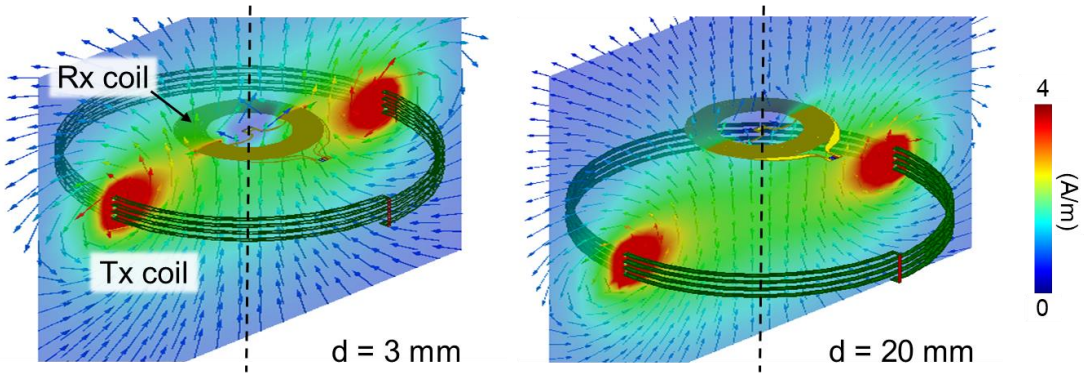

Supplementary Fig. 6 | Long-range electromagnetic characteristics of bioresorbable, leadless cardiac pacemakers.

Simulated electromagnetic field distribution near the coupled Rx and Tx coils for a separation distance of (left) 3 mm and (right) 20 mm (transmitting power = 1 W).

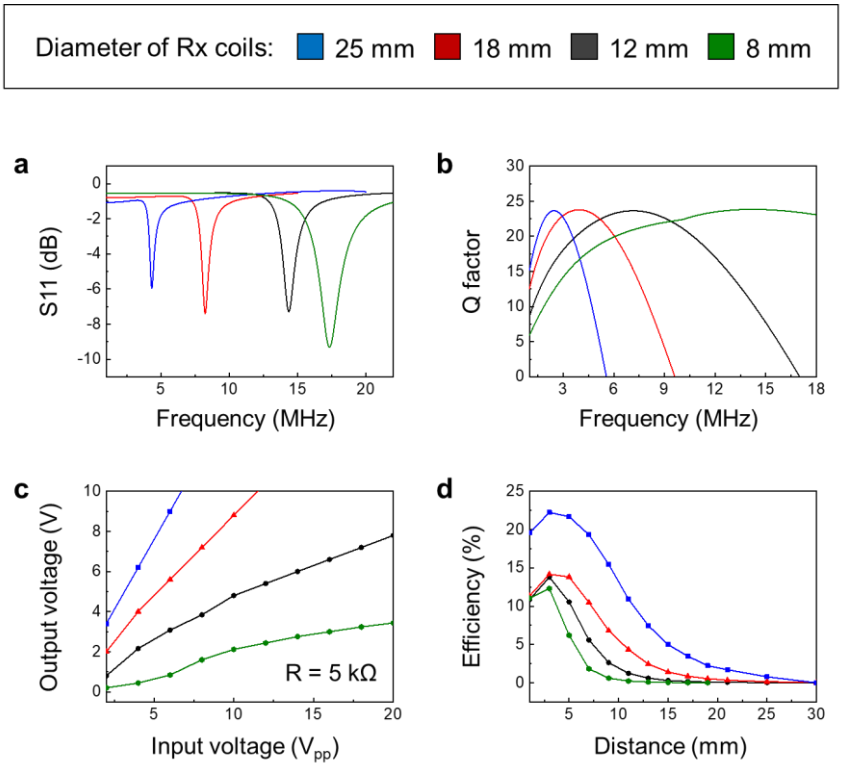

Supplementary Fig. 7 | Electromagnetic characteristics of bioresorbable, leadless cardiac pacemakers with various sizes of wireless power harvesting units.

The sizes of the Rx coils are 25 (blue), 18 (red), 12 (black), and 8 mm (green). **a,** Simulated scattering parameters (S11) of the wireless power harvesting units with different sizes of receiver coils. The resonance frequency of each coil is 4.24, 8.03, 13.91, 17.33 MHz, respectively. **b,** Simulated Q factors of the wireless power harvesting units, respectively. **c,** Experimental results for the output voltage as a function of input voltage at a coil-to-coil distance of ~1 mm and load resistance of 5 kΩ. **d,** Simulated power transfer efficiency as a function of changes in coil-to-coil distance.

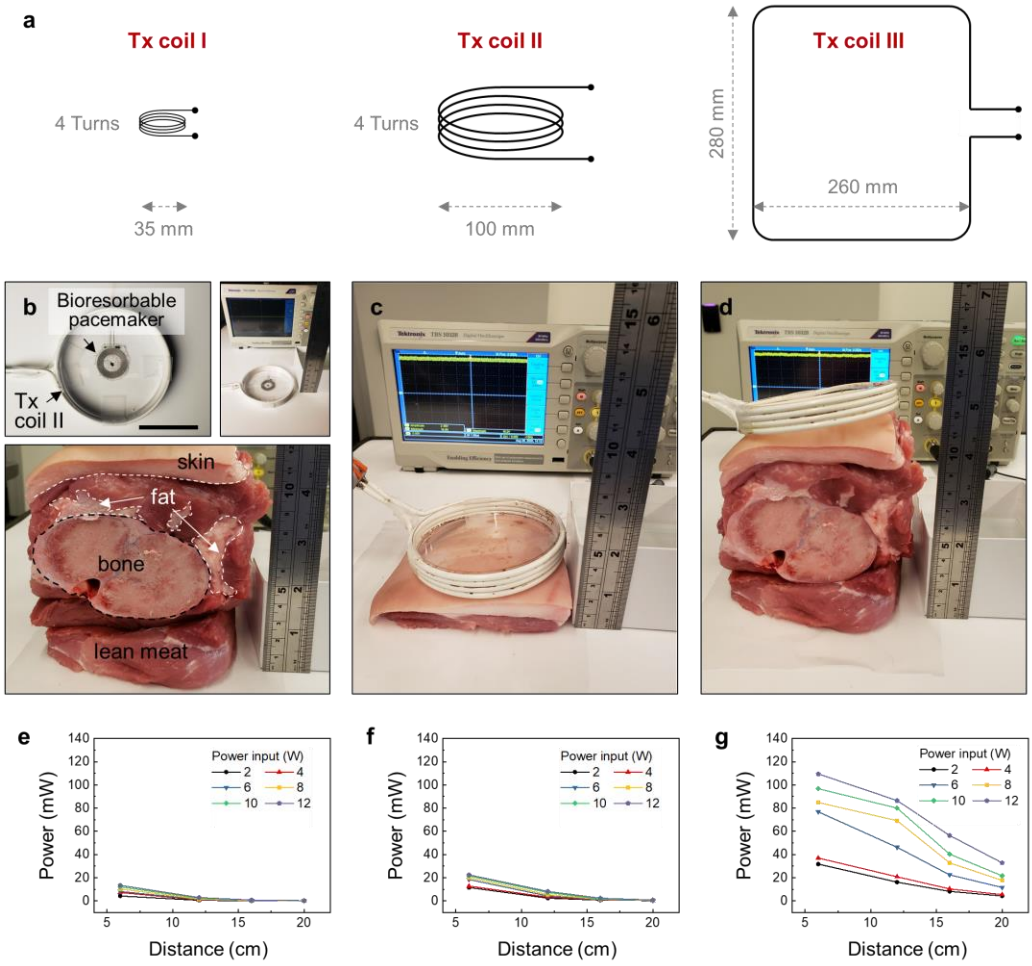

Supplementary Fig. 8 | *In vitro* long-range wireless operation test of a bioresorbable cardiac pacemaker system.

a, Schematic illustrations of three different designs of Tx coil: (i) Tx coil I (solenoid type; 4 turns; 35 mm diameter); (ii) Tx coil II (solenoid type; 4 turns; 100mm diameter); Tx coil III (square; 1 turn; 260 × 280 mm^2). **b**, (top left) Photograph of bioresorbable pacemaker (diameter of Rx coil = 25 mm) and Tx coil II. Scale bar, 50 mm. (top right) Experimental setup for measurement of long-range operation. Fixing the position of the bioresorbable pacemaker and changing the position of the Tx coil represents the method used to change the coil-to-coil distance. (bottom) Cross-sectional image of a slice of porcine tissue (~120 mm thick) that includes skin, fat, bone, and muscle. **c**, Wireless energy transfer through slices of porcine tissue with thicknesses of 20 mm. The oscilloscope indicates an open circuit voltage of 16.8 V (Input power = 2 W; input frequency = 13.56 MHz). **d**, Wireless energy transfer through slices of porcine tissue with thicknesses of 120 mm. The oscilloscope indicates an open circuit voltage of 16.8 V (Input power = 12 W; input frequency = 13.56 MHz). **e-g**, Changes in output power of the bioresorbable pacemaker as a function of coil-to-coil distance (input frequency = 13.56 MHz; Input power = 2-12 W; load resistance = 5000 Ω): (e) Tx coil I; (f) Tx coil II; (g) Tx coil III.

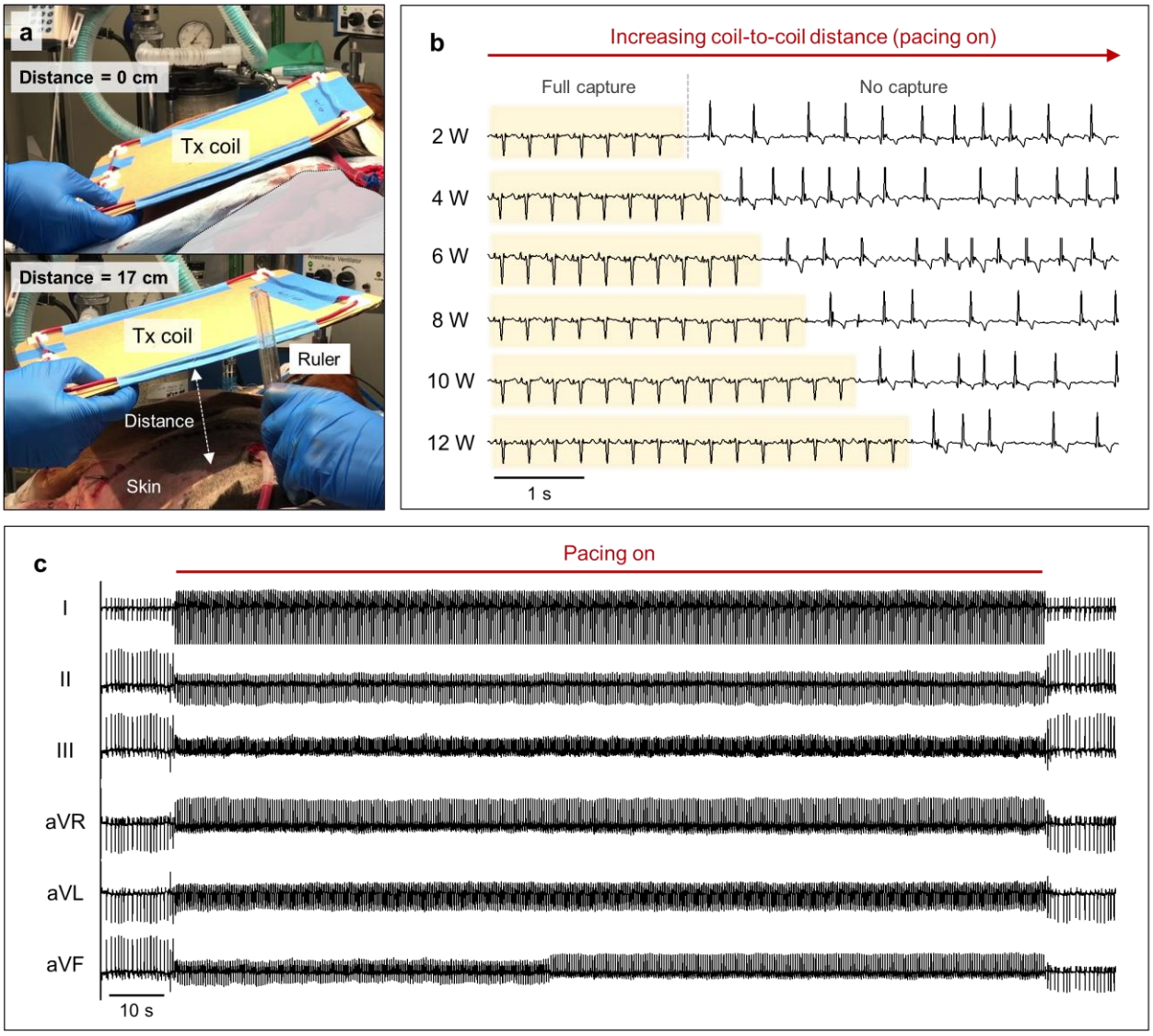

Supplementary Fig. 9 | *In vivo* demonstration of a long-range wireless operation capabilities of bioresorbable cardiac pacemaker system in an *in vivo* canine model.

a, Photograph of long-range operation test setup with coil-to-coil distance of (top) 0 cm and (bottom) 17 cm. Measuring the maximum distance for pacing between the surface of skin and the Tx coil (Tx coil III; square; 1 turn; 260 × 280 mm^2) defines the long-range wireless energy transfer capability of this system. **b,** Changes in ECG with increasing coil-to-coil distance and input power (2-12W; burst period = 300 ms; pulse width = 5 ms). Transition of ECG signal from ventricular capture (yellow background; ~200 bpm) to intrinsic rhythm (atrial fibrillation; white background; ~120 bpm) defines the maximum distance for pacing. n = 3 biologically independent animals per group. **c,** 6-lead ECG recording of continuous pacing (pacing time = ~ 2 min.; input power = 4 W; skin-to-Tx coil distance = 10 cm) in the operation room. n = 3 biologically independent animals per group.

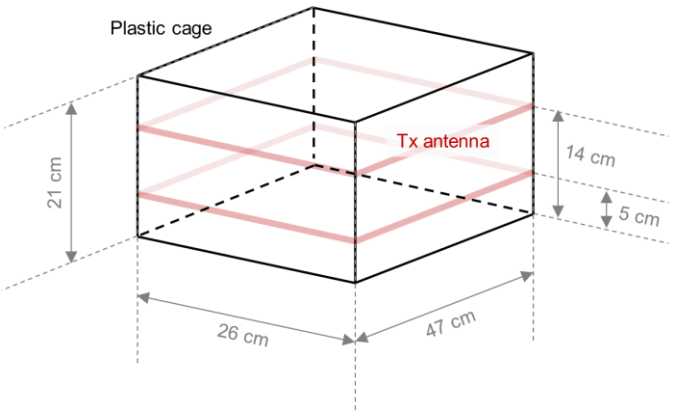

Supplementary Fig. 10 | Setup for continuous, *in vivo* stimulation, with dimensions.

A custom-built plastic cage outfitted with Tx antennas provides a region within which the animal outfitted with an implanted device can freely move about for continuous *in vivo* pacing of the heart.

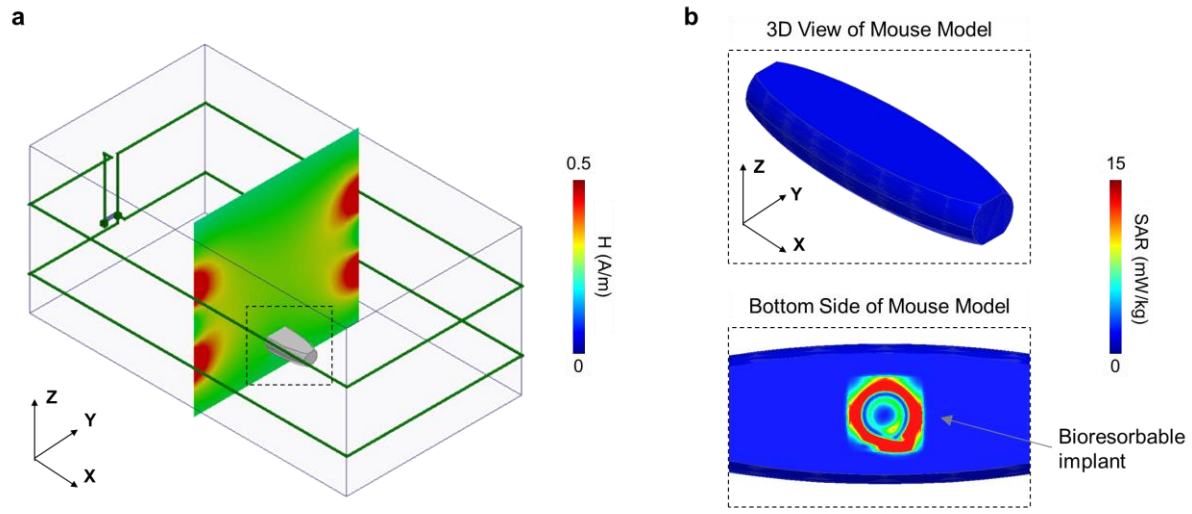

Supplementary Fig. 11 | Results of simulation of the distribution of the electromagnetic field

a, Magnetic field distribution inside the cage at a cross sectional plane that intersects a simple model of a mouse. **b,** Simulated specific absorption rate (SAR; a measure of the rate at which RF energy is absorbed by the body) as a function of position across a mesh model of a mouse body. (top) 3D and (bottom) 2D (x,y-axis) view of the mouse model.

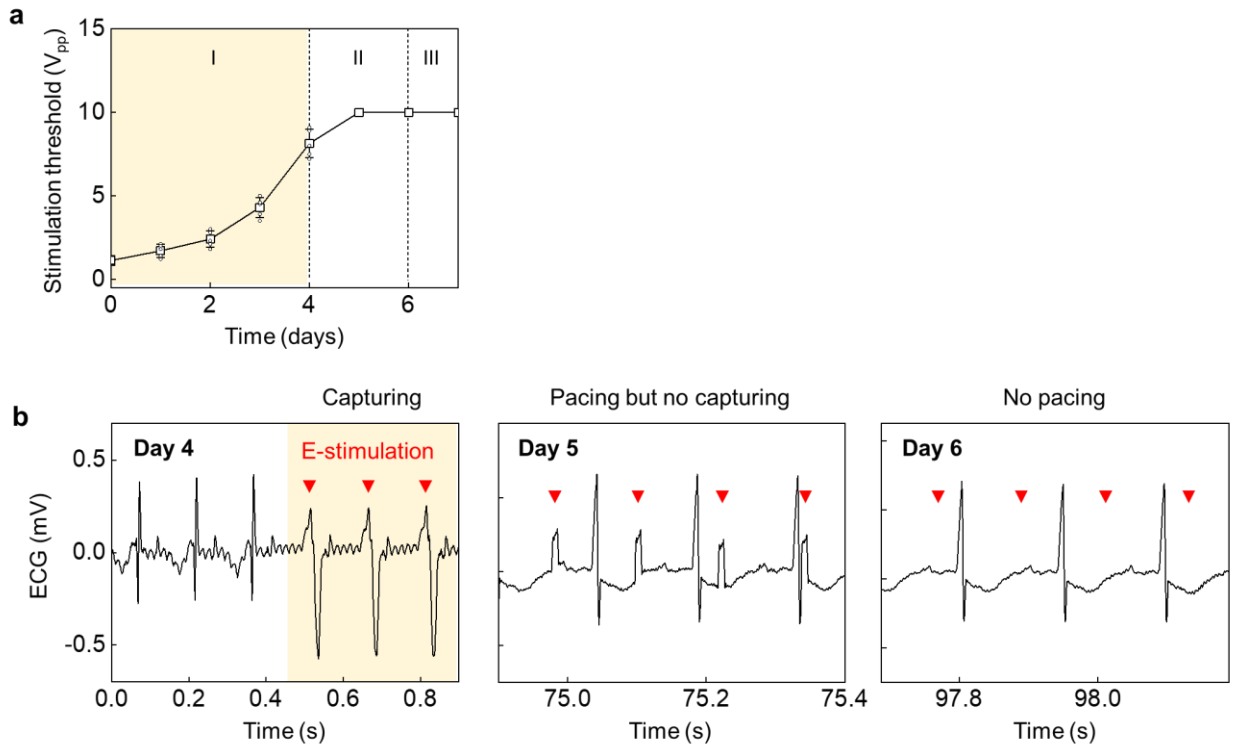

Supplementary Fig. 12 | Changes in wireless pacing behavior during *in vivo* chronic tests in a rat model.

a, Changes in stimulation threshold (i.e. minimum input voltage to Tx coil for pacing) as a function of time after implantation. Phase I, II, and III indicate the pacing behavior: capture, pacing but no capture, and no pacing, respectively. n = 5 biologically independent animals. **b,** ECG signals from rats with implanted bioresorbable cardiac pacemakers at 4, 5 and 6 days after device implantation. Red triangles indicate the timing of wireless electrical stimulation. n > 10 biologically independent animals per group. In **a**, the results are shown as means ± s.e.m.

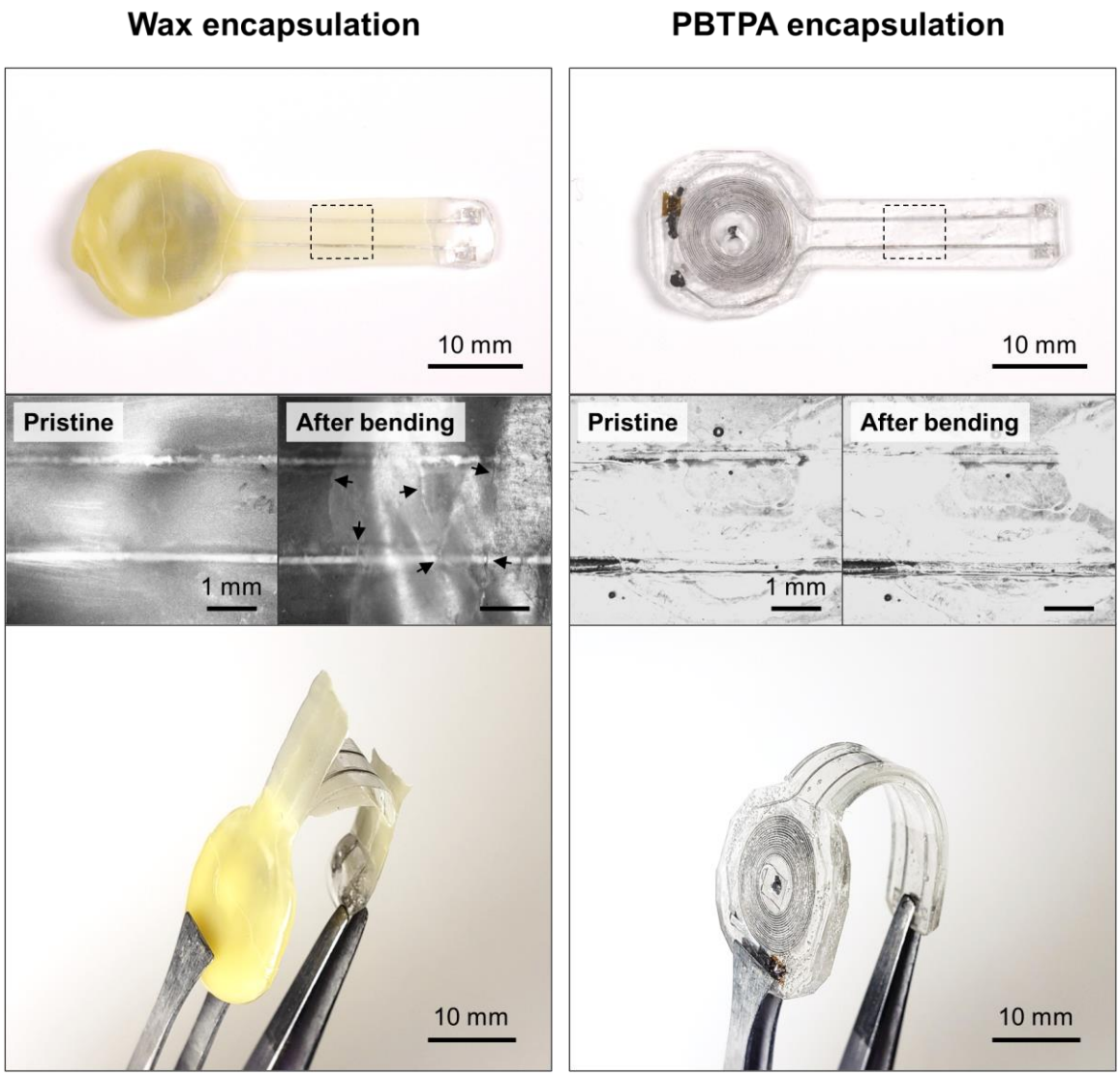

Supplementary Fig. 13 | Experimental studies of mechanical reliability of polymer-encapsulated bioresorbable, leadless cardiac pacemakers.

The devices are encapsulated by (left) Candelilla wax and (right) polybuthanedithiol 1,3,5-triallyl-1,3,5-triazine-2,4,6(1H,3H,5H)-trione pentenoic anhydride (PBTPA). (top) Photographs of encapsulated devices after fabrication. (middle) Optical microscope images of the polymer encapsulated extension electrode (left) before and (right) after bending (bend radius = 10 mm). Arrows indicate cracks. (bottom) Photographs of polymer encapsulated devices under mechanical deformation (bend radius = 5 mm).

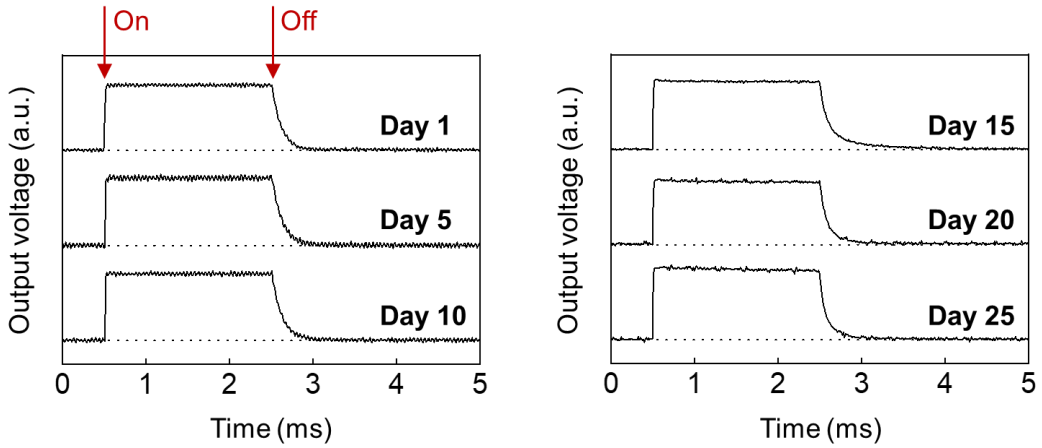

Supplementary Fig. 14 | Functional lifetime of the bioresorbable cardiac pacemaker with an encapsulating structure formed with a polyanhydride (PBTPA) material.

During immersion in bovine serum at 37 °C over the course of several weeks, the output voltage of the encapsulated bioresorbable pacemaker during wireless operation remains consistent.

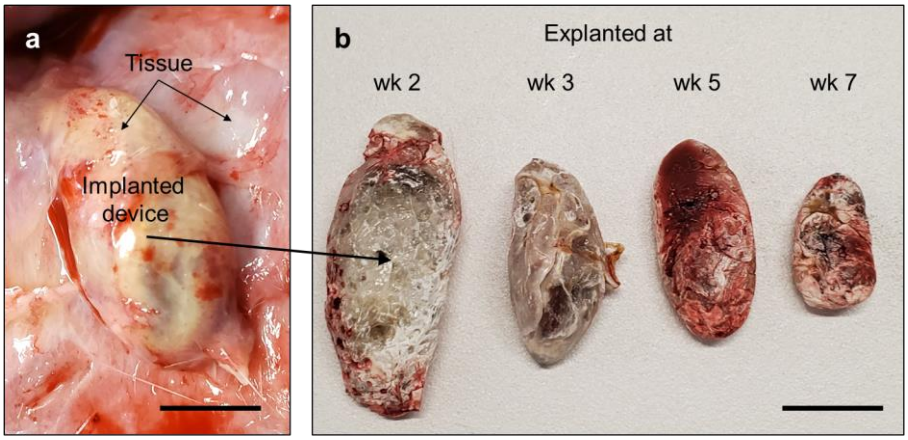

Supplementary Fig. 15 | *In vivo* studies of degradation of the bioresorbable, leadless cardiac pacemaker.

a, Image of device after 2 weeks of implantation in a rat model. Scale bar, 10 mm. **b,** Images of explanted devices at different stages of bioresorption over the course of 7 weeks. Scale bar, 10 mm.

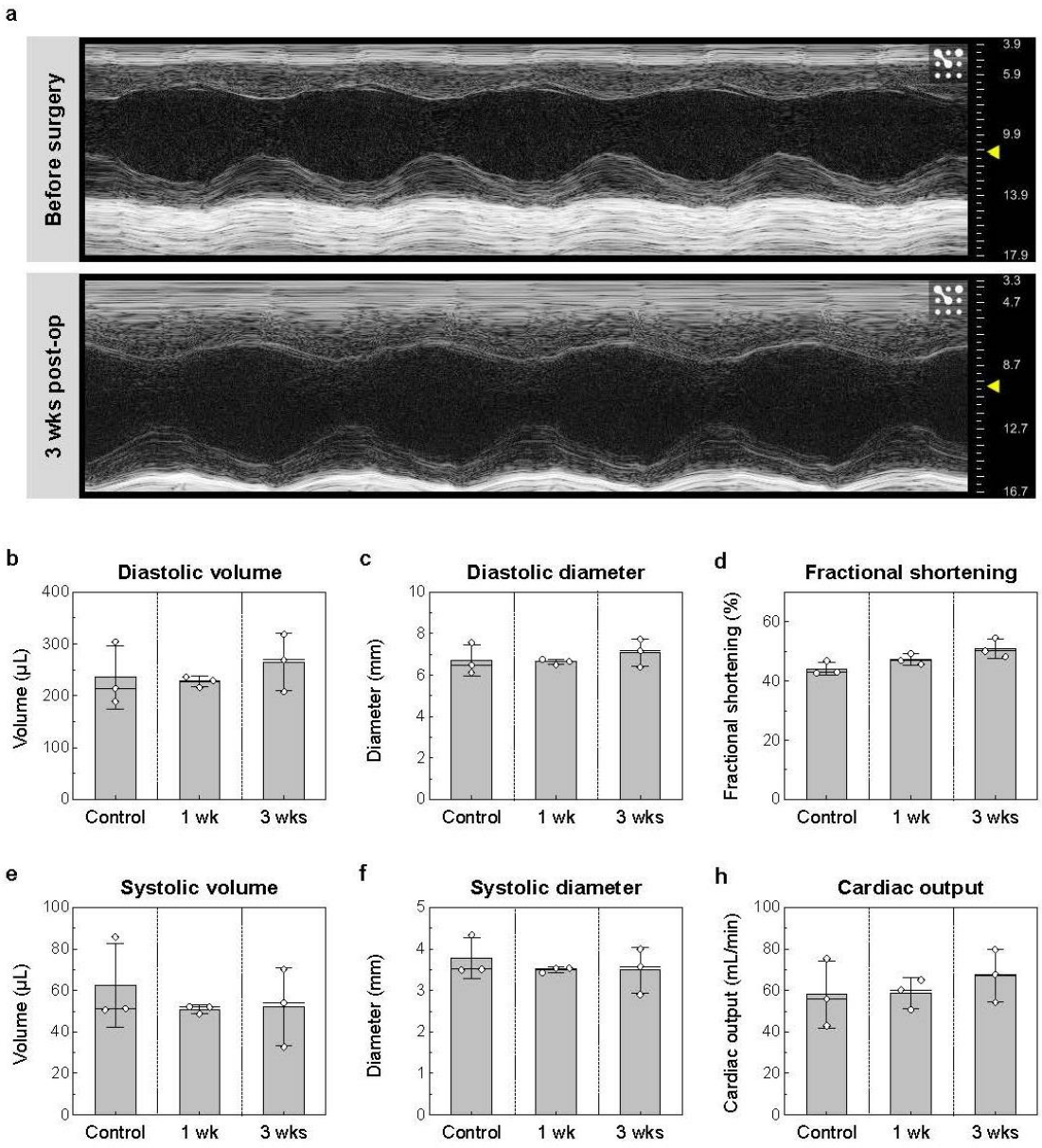

Supplementary Fig. 16 | Echocardiographic assessment of animals following pacemaker implantation.

a, M-mode echocardiogram (top) before and (bottom) after surgery. **b-h,** No significant changes in diastolic volume, diastolic diameter, fractional shortening, systolic volume, systolic diameter, or cardiac output when compared before or at 1 or 3 weeks following operation. Friedman's test: diastolic volume ($\chi_F^2(2)$ = 0.000, P > 0.9999), diastolic diameter ($\chi_F^2(2)$ = 0.000, P > 0.9999), fractional shortening ($\chi_F^2(2)$ = 2.667, P = 0.3611), systolic volume ($\chi_F^2(2)$ = 0.6667, P = 0.9444), systolic diameter ($\chi_F^2(2)$ = 0.6667, P = 0.9444), cardiac output ($\chi_F^2(2)$ = 2.000, P = 0.5278). Dunn's multiple comparison test at a significance level of 0.05. n = 3 biologically independent animals.

These measurements show that implementation of the device does not impair the mechanical function of the heart. Data are presented as mean values ± SD.

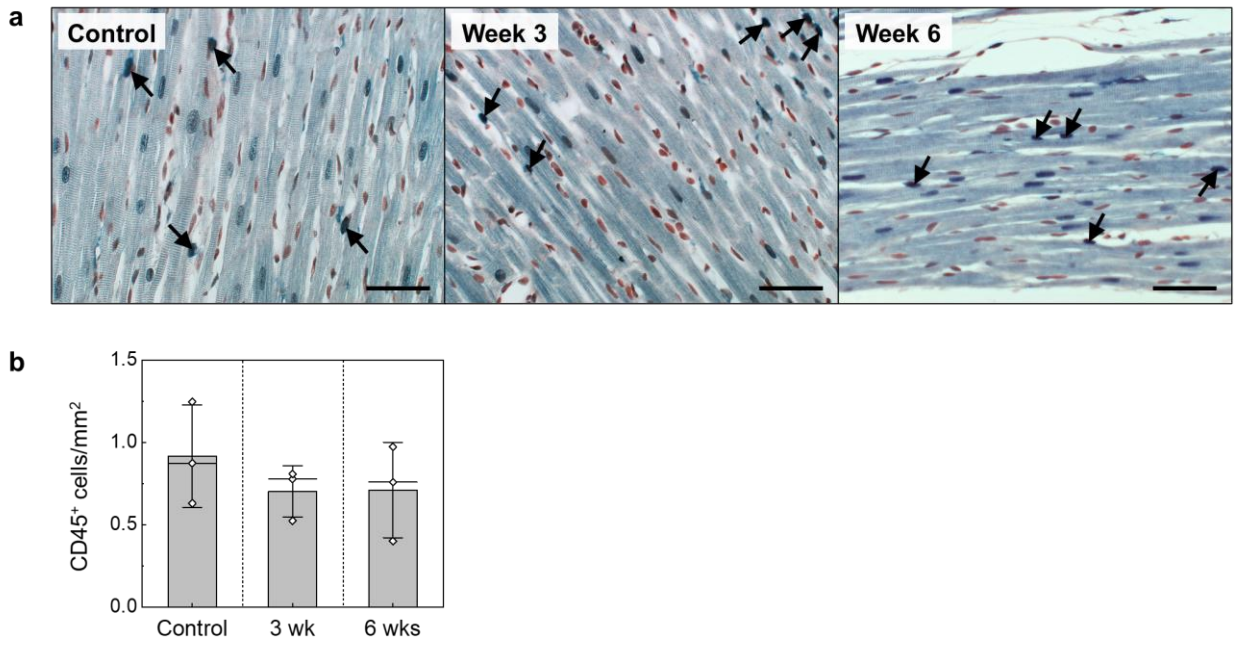

Supplementary Fig. 17 | Inflammatory response of myocardium following pacemaker implantation.

a, Representative images of the stained cross-sectional area of the left ventricle of a rat without (control) and with an implanted device after 3 weeks and 6 weeks near the site of implantation. Arrowheads indicate $CD45^+$ cells. Scale bar, 50 µm. **b,** Frequency of $CD45^+$ cells in the ventricular myocardium near the site of implantation. No significant difference in $CD45^+$ cells in the myocardium following pacemaker implantation. Kruskal-Wallis test, $H(2) = 1.067$, $P = 0.6643$. Dunn's multiple comparison test at a significance level of 0.05. $n = 3$ biologically independent animals per group. Data are presented as mean values ± SD.

Reference

1. Caverly, R. H. & Hiller, G. The frequency-dependent impedance of p-i-n diodes. *IEEE Trans. Microw. Theory Tech.* **37**, 787–790 (1989).

2. Youbok Lee. Antenna Circuit Design for RFID Applications. in *microID® 13.56 MHz RFID System Design Guide* 210 (Microchip, 2004).

3. Lau, E. W. *Leads and Electrodes for Cardiac Implantable Electronic Devices*. *Clinical Cardiac Pacing, Defibrillation and Resynchronization Therapy* (Elsevier Inc., 2017). doi:10.1016/b978-0-323-37804-8.00011-0.

4. Iravanian, S., Herndon, C., Langberg, J. J. & Fenton, F. H. Theoretical Modeling and Experimental Detection of the Extracellular Phasic Impedance Modulation in Rabbit Hearts. *Front. Physiol.* **10**, 883 (2019).

5. Fallert, M. A. *et al.* Myocardial electrical impedance mapping of ischemic sheep hearts and healing aneurysms. *Circulation* **87**, 199–207 (1993).

6. Schwartzman, D., Chang, I., Michele, J. J., Mirotznik, M. S. & Foster, K. R. Electrical Impedance Properties of Normal and Chronically Infarcted Left Ventricular Myocardium. *J. Interv. Card. Electrophysiol.* **3**, 213–224 (1999).

7. Rong, C. *et al.* Analysis of wireless power transfer based on metamaterial using equivalent circuit. *J. Eng.* **2019**, 2032–2035 (2019).

8. Koo, J. *et al.* Wireless bioresorbable electronic system enables sustained nonpharmacological neuroregenerative therapy. *Nat. Med.* **24**, 1830–1836 (2018).

9. Choi, Y. S. *et al.* Biodegradable Polyanhydrides as Encapsulation Layers for Transient Electronics. *Adv. Funct. Mater.* **30**, 2000941 (2020).